Differential nuclear-spin-dependent light shifts and state mixing of Rydberg atoms

H. Nguyen, J. Lampen, P. R. Berman, and A. Kuzmich
Department of Physics, University of Michigan, Ann Arbor, Michigan 48109, USA

(Received 9 April 2019; revised manuscript received 3 July 2019; published 18 September 2019)

In this paper we present a detailed analysis of the nuclear-spin manifolds associated with the *ns* Rydberg levels of ^{87}Rb atoms that interact with both magnetic and optical lattice fields. Eigenvalues and eigenkets for the Rydberg manifold are obtained and used to study the dynamics of phase-matched emission following illumination of an ensemble of cold atoms with excitation and readout laser pulses. By comparing the measured emission signal to predictions of a model that accounts for the quantized motion of atoms in a one-dimensional optical lattice potential, we are able to extract the Rydberg hyperfine and light shift contributions to the observed modulation frequencies. In this way the hyperfine splitting of Rydberg *ns* levels is measured for n in the range of 30 to 65. Our results should be relevant for realizations of high-fidelity Rydberg qubits confined in optical potentials.

DOI: 10.1103/PhysRevA.100.033412

I. INTRODUCTION

A promising platform for quantum information processing is based on the excitation of ultracold atoms to Rydberg states [1]. Achieving long-lived ground-Rydberg atomic coherence is one of the cornerstones of this approach. To suppress the effects of motional dephasing on this coherence, the atoms can be confined in optical potentials that are identical for the ground and Rydberg states [2–8]. However, in addition to confining the atoms, the optical trap fields also mix and shift the Rydberg energy levels. As a consequence, the energy level spacing within a given Rydberg manifold results from a complicated combination of optical field potentials, hyperfine interactions, and interactions of the atoms with any external magnetic bias fields. A complete understanding of this level structure is needed to maximize the fidelities for quantum information protocols using trapped Rydberg atoms.

In this paper we present a theoretical and experimental study of ^{87}Rb Rydberg atoms confined in an optical lattice potential and subjected to an external magnetic field. For a given n, the frequency of the lattice fields is chosen so as to match the light shift potentials for the ground and *ns* Rydberg levels [5,8]. Actually, it is not possible to match the ground-state lattice potential to that of *all* the hyperfine sublevels in a given *ns* level. For example, an *ns* level of ^{87}Rb contains eight sublevels. In general, the trapping potential differs for each of these levels and must be accounted for in a complete analysis. Moreover, since the atoms are trapped in these potentials, it becomes necessary to use a fully quantum theory for the atomic motion.

The trapped atoms are subjected to a two-photon pulse that excites the atoms to a targeted Rydberg level, followed by a time-delayed readout pulse that leads to phase-matched emission from the sample. By a proper choice of excitation field polarization, the output signal, measured as a function of the time delay, contains components that oscillate at the frequency separations of the *ns* Rydberg sublevels.

These frequency separations contain contributions arising from the magnetic-field interaction, hyperfine interaction, and light shift potentials. To isolate these effects, we calculate the eigenkets and eigenenergies of the Rydberg levels in the *absence* of light shifts and then determine to what extent the light shifts modify them. The light shifts themselves are composed of near-resonance and ponderomotive contributions. The ponderomotive contribution, which includes effects related to the breakdown of the dipole approximation [6], is a function of n, but, for a given n, is the same for all the sublevels. The near-resonance contribution both shifts and couples the sublevels. Rather remarkably, we find that coupling of hyperfine–magnetic-field eigenkets is almost negligible for the range of our experimental parameters, although there was no *a priori* reason to believe that this should be the case when the lattice field polarization is orthogonal to the magnetic field. As a result, the only effect of the optical potential is to provide a differential shift for the Rydberg sublevels. We are able to assess the role played by these differential light shifts and to determine what effect, if any, they have on the atomic motion. In this way we determine the hyperfine constant A from the measured frequency intervals for n ranging from 30 to 65. Previously, A values were measured for low values of n using direct optical spectroscopy [9,10]. In these experiments, residual Doppler broadening resulted in a spectral resolution to about 100 kHz, limiting the method to $n \leqslant 27$. Millimeter-wave spectroscopy has been used for high-n states of atomic Cs, with kHz-level resolution achieved using ultracold atoms [11]. In this work we achieve a resolution as low as several kHz.

II. EXPERIMENT

The experimental setup and level diagram for one of our excitation schemes are shown in Fig. 1. For the most part, the experimental setup is identical to the one used in our previous work [8]. The major difference is that the polarization of the field Ω_1 in the current experiment has both y and z components, whereas it was z polarized in the previous experiment. An ultracold sample of Rb atoms is loaded into a

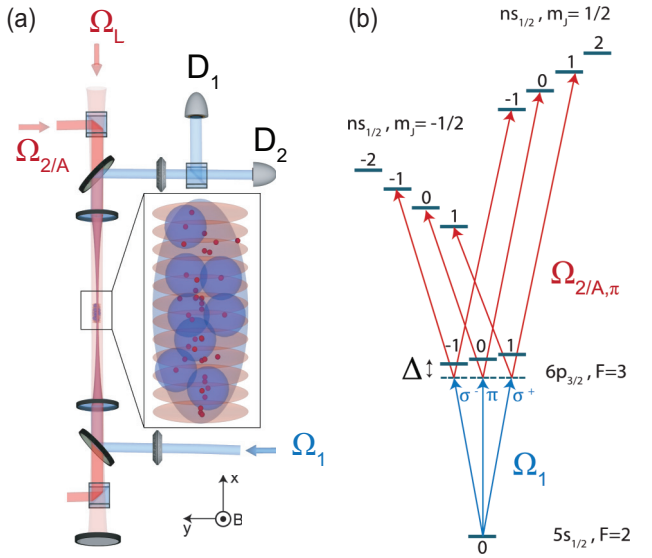

FIG. 1. (a) Experimental setup. An ultracold sample of ^{87}Rb gas is trapped in a "magic" one-dimensional optical lattice formed by a retroreflected lattice beam Ω_L that is directed along the x axis and polarized in the y direction. Two excitation beams, Ω_1 (420 nm) and Ω_2 (varying between 1013 nm and 1026 nm) counterpropagate along the x axis and are focused at the position of the atomic sample cloud with ($\frac{1}{e^2}$) waists of 17 and 15 μm, respectively. After a time delay T_s following the excitation pulse, a retrieval field Ω_A generates a phase-matched output signal. The polarization of field Ω_2 and the retrieval field Ω_A is fixed in the z direction, whereas the polarization of field Ω_1 has both y and z components that are adjusted to optimize the modulation depth of the output signal. The output signal has both y and z components which are mixed with a half-wave plate, split by a polarizing beam splitter, and measured by single-photon detectors $D_{1(2)}$. (b) Atomic level diagram showing the initial ($|5s_{1/2}, F = 2, m = 0\rangle$) state, intermediate ($|6p_{3/2}\rangle$), and Rydberg $|ns_{1/2}\rangle$ sublevels. The final state manifold consists of two spectrally resolved Zeeman submanifolds, each containing four levels. Even in the presence of light shifts, $m_F = m_J + m_I$ remains a good quantum number. For this excitation scheme, the $m_F = 0, \pm 1$ levels in each electronic Zeeman manifold are populated.

one-dimensional optical lattice formed by counterpropagating optical fields polarized along the y axis. The measurements are made using a magnetic field $B = 5$ G for which the electronic Zeeman splitting is much greater than the hyperfine separations of the ns levels being studied, the so-called hyperfine Paschen-Back regime. In this case the $ns_{1/2}$ Rydberg level splits into two manifolds, characterized by $m_J = \pm 1/2$, separated in frequency by $\approx$14 MHz, with each manifold consisting of four m_I components. The $\sim$1 MHz two-photon excitation bandwidth $\delta\nu$ is much smaller than the frequency separation between the two manifolds. The lattice wavelength $\lambda \simeq$ 1012–1027 nm is tuned to near resonance with the $|6p_{3/2}\rangle \leftrightarrow |ns_{1/2}\rangle$ atomic transition, the specific value chosen to match the optical potentials for the ground state and the $m_F = m_J + m_I = 0$ component of the Rydberg Zeeman manifold.

The ensemble is driven resonantly to the Rydberg state $|ns_{1/2}\rangle$ using counterpropagating, $T_e = 1$ μs-long pulses of a 420 nm field Ω_1 and a (nominally) 1012 nm field Ω_2. The polarization of Ω_1, controlled by a half-wave plate oriented at an angle $\theta_i/2$ with respect to the z axis, is a linear combination of the y and z polarizations, while Ω_2 is purely z polarized. In this way three m_I components in a given electronic Zeeman manifold of $|ns\rangle$ are excited. After a storage period T_s, the atoms are coherently driven by a (z-polarized) 10-μs-long retrieval field Ω_A whose frequency is resonant with the $|ns\rangle \leftrightarrow |6p_{3/2}\rangle$ transition. The ensuing cooperative emission on the $|6p_{3/2}\rangle \leftrightarrow |5s_{1/2}\rangle$ transition is directed through a half-wave plate and polarizing beam splitter. Each of the output polarization modes is collected into a single-mode fiber and directed onto a single-photon detector.

III. THEORY

The theoretical analysis is carried out in two stages. First we calculate the energy of the sublevels of an ns Rydberg state of ^{87}Rb subjected to a magnetic field **B** along z and a y-polarized optical trap field whose frequency is nearly resonant with the $|ns\rangle \leftrightarrow |6p_{3/2}\rangle$ transition frequency. We then use this result to obtain an expression for the phase-matched signal as a function of delay between excitation and retrieval pulses. The details of the calculation are presented in the Appendix. Here we summarize some of the results.

In the absence of all but the Coulomb interaction, there are eight degenerate states in an ns manifold that can be labeled as $|nLSJIFm_F\rangle$ with $S = 1/2$ and $I = 3/2$. The energy levels in a given Rydberg ns manifold are determined by the hyperfine interaction, the magnetic-field interaction, and the optical potentials produced by the trap field. In a given basis, these interactions result in a shift and coupling of the various Rydberg sublevels. In principle, it is necessary to diagonalize the Hamiltonian associated with a given ns manifold to obtain the eigenenergies and eigenkets. For our experimental parameters, however, the eigenkets that are obtained are approximately those in which the optical potentials are set equal to zero. As such, $m_F = m_J + m_I$ corresponds to an approximate constant of the motion. We denote the zero field hyperfine separation of the ns state by $h\nu_{hfs}$ (the n label is suppressed). It is a simple matter to obtain the eigenkets and eigenfrequencies ω_{nsm_F} of the ns levels in the absence of the trap field.

The optical potentials produced by the trap field can be broken down into two contributions. First there is the ponderomotive potential associated with the A^2 (**A** is the vector potential of the trap field) contribution to the Hamiltonian and is the same for all the levels in the ns Rydberg manifold. In addition, there is also the $\mathbf{A}\cdot\mathbf{p}$ contribution. Although the trap field is in near-resonance with the $|ns\rangle \leftrightarrow |6p_{3/2}\rangle$ transition, the detuning of the trap field frequency from the $|ns\rangle \leftrightarrow |6p_{3/2}\rangle$ transition frequency is *not* sufficiently large to justify the neglect of the hyperfine splitting of the $6p_{3/2}$ sublevels. This results in optical potentials that are dependent on the m_F values of the ns Rydberg sublevels.

For magic wavelength lattices, one matches the ground- and excited-state trap potentials by a proper choice of the trap field detuning. In our case, it is *not* possible to simultaneously match the potentials for *all* the Rydberg sublevels. With an external magnetic-field strength of about 5 G, an ns manifold

consists of two Zeeman submanifolds (corresponding to $m_s = \pm 1/2$) separated by about 14 MHz, each containing four of the eight sublevels of the *ns* Rydberg levels. As such, the excitation fields can be chosen to excite only one of these Zeeman submanifolds (see Fig. 1). For a given Zeeman submanifold, we match the $m_F = 0$ potential to the ground-state potential. The trap potential for the other Zeeman sublevels will then differ from the ground-state potential.

Both the near-resonant and ponderomotive components of the Rydberg optical potentials, as well as the ground-state optical potential, contain both lattice and nonlattice contributions. The lattice contributions are responsible for trapping the atoms longitudinally in the wells of the potential. The remaining nonlattice contributions to the optical potentials trap the atoms in the transverse direction and give rise to a spatially inhomogeneous shift of the levels owing to the transverse spatial dependence of the trap fields. The lattice potentials determine the center-of-mass motion of the atoms. Since these potentials are state dependent, the motion must be treated quantum mechanically. The spatial dependence of the nonlattice potentials results in a dephasing that degrades the output signal with increasing time delay between the excitation and retrieval pulses.

The atoms are optically pumped into a *single* magnetic sublevel having angular momentum $F = 2$ and magnetic quantum number $m_F = 0$. Pulsed, counterpropagating fields incident along the x direction drive a two-photon transition from this ground state to the Zeeman manifolds of an *ns* Rydberg level. The first excitation field propagates in the $\mathbf{u}_x$ direction, has polarization given by $\cos\theta_i \mathbf{u}_z + \sin\theta_i \mathbf{u}_y$, and is nearly resonant (but still far enough from resonance to neglect any saturation effects) with the transition from the ground state to a single hyperfine state of either the $6p_{3/2}$ or $5p_{1/2}$ manifolds (manifolds specified by the symbol p_J), depending on the excitation scheme. The detuning Δ in Fig. 1(b) is of order $\Delta/2\pi \approx 12$ MHz and the frequency spacing of adjacent $6p_{3/2}(F = 3)$ magnetic sublevels is ≈4.7 MHz. The second, counterpropagating field couples each intermediate-state magnetic sublevel labeled by m_F to a single level in either the upper ($m_J = 1/2$) or lower ($m_J = -1/2$) Zeeman submanifold having the same value of m_F.

The excitation pulses create coherence between the $F = 2$, $m_F = 0$ ground level and the Rydberg sublevels. To monitor this coherence, a retrieval pulse, polarized in the z direction and propagating in the $-\mathbf{u}_x$ direction, is applied at a time T_s following the excitation pulses. The field is resonant with the same Rydberg–intermediate-state transition used in the excitation process. The excitation, readout, and vacuum fields combine to produce a phase-matched output field in the $\mathbf{u}_x$ direction that has both y and z polarization components. These components are mixed on a half-wave plate to produce new vertical and horizontal components which are then separated by a polarizing beam splitter and measured in two detectors.

It is shown in the Appendix that the signal at time T_s normalized to that at $T_s = 1\ \mu$s, the vertical signal component, can be written as

$$\eta_V(T_s) = S_V(T_s)/S_V(T_s = 1\mu s), \tag{1}$$

where

$$S_V(T_s) = \left| \int_{-\infty}^{\infty} dX \int_0^{\infty} \rho\, d\rho \Lambda(\rho, X)\mathcal{N}(\rho, X) C_V(\rho, X, T_s) \right|^2 \times e^{-\Gamma_{ns} T_s}, \tag{2}$$

$$C_V(\rho, X, T_s) = \sum_{m_F=-1}^{2} \sum_{q,q'}^{q_{\max}} e^{-i\omega_{nsm_F} T_s} Q^{(V)}_{p_J nsm_F} \times e^{-2\pi i \tilde{D}^{(j)}_{nsm_F}(\rho,X) T_s} M_{gq;nsm_F q'}(-k) \times M_{nsm_F q';gq}(k) e^{i(\omega_q^{(g)} - \omega_{q'}^{(nsm_F)}) T_s} \rho_{1q,1q}(0), \tag{3}$$

$\Lambda(\rho, X)$ is proportional to the product of the spatially dependent Rabi frequencies of the excitation and retrieval pulses and $\mathcal{N}(\rho, X)$ is the atomic density distribution. A loss factor, $e^{-\Gamma_{ns} T_s/2}$, has been added to allow for decay between the excitation and retrieval pulses owing to spontaneous emission, blackbody radiation, and decay from the intermediate state.

The factor $C_V(\rho, X, T_s)$ reflects the contributions to the signal from different initial motional states in the ground-state lattice potential, represented by density-matrix elements $\rho_{1q,1q}(0)$. Here ω_{nsm_F} are eigenfrequencies of the Hamiltonian that account for differential light shifts, in addition to the magnetic and hyperfine interactions. The frequencies $\omega_q^{(g)}$ and $\omega_{q'}^{(nsm_F)}$ are those associated with the ground and nsm_F lattice potentials, respectively, while $\tilde{D}^{(j)}_{nsm_F}(\rho, X)$ is the spatially dependent difference in nonlattice potentials between nsm_F and ground-state levels. The matrix elements $M_{nsm_F q';gq}(k)$ represent the coupling between the ground and Rydberg motional states, while the function $Q^{(V)}_{p_J nsm_F}$ incorporates all the excitation and retrieval dynamics. The sums over q, q', q'' are restricted to (quasibound) states; that is, $q_{\max}$ is the number of bound states in the potential.

IV. ANALYSIS OF RETRIEVED SIGNAL

Let us first consider the data for $n = 40$. As a function of delay time T_s between the excitation and readout pulses, the overall signal decays, primarily as a result of blackbody-induced transitions and spontaneous decay. In addition to the overall decay, the signal exhibits an oscillatory behavior. If the trap potentials are purely harmonic characterized by frequency ω and if the ground and Rydberg potentials are matched, for a ground-state thermal distribution,

$$\rho_{1q,1q}(0) = (1 - e^{-\beta}) e^{-q\beta}, \quad \beta = \frac{\hbar\omega}{k_B T}, \tag{4}$$

the quantity C_V in Eq. (3) can be written in the form [12]

$$|C_V(T_{21})| \approx e^{-2\zeta^2[1-\cos(\omega T_s)]/\beta} \left| 1 + Q_1 e^{-i\omega_{10} T_s} + Q_{-1} e^{-i\omega_{-10} T_s} \right|, \tag{5}$$

where

$$\zeta = k_{12} \sqrt{\frac{\hbar}{2M\omega}} \tag{6}$$

is the Lamb-Dicke parameter for the excitation field (k_{12} is the effective propagation constant for the two-photon excitation field and M is the atomic mass) and ω_{m0} ($m = -1, 1$) is the

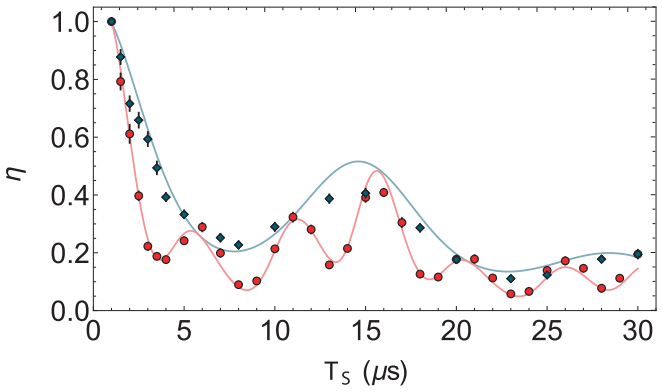

FIG. 2. Normalized signal $\eta \equiv S(T_s)/S(T_s = 1\ \mu\text{s})$ as a function of storage time for principal quantum number $n = 40$ with fitted trap depth $U_0/k_B = 31\ \mu$K and temperature $T = 10\ \mu$K for a single excited state (blue) and a triplet of states (red) using $(\theta_i, \theta_d) = (0^\circ, 24^\circ)$ and $(32^\circ, 24^\circ)$, respectively. Solid curves are based on our theoretical model.

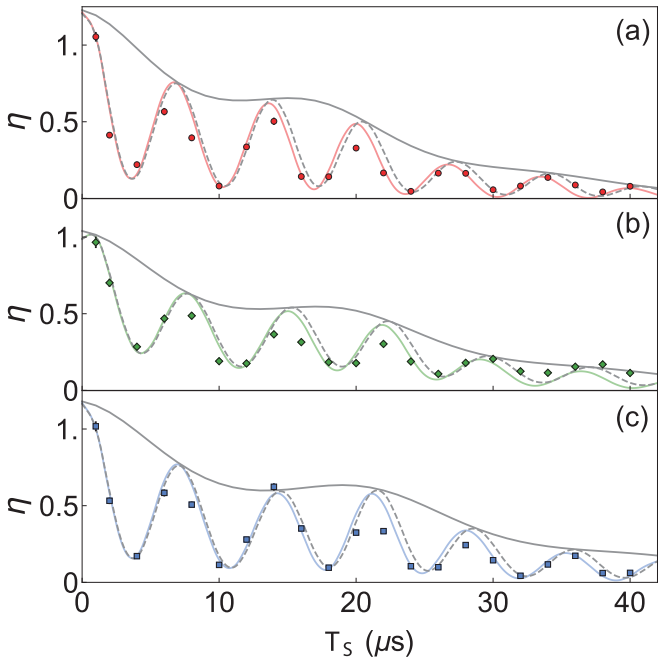

FIG. 3. Normalized signal η utilizing the alternative excitation scheme via the intermediate $|5p_{1/2}\rangle$ state and $(\theta_i, \theta_d) = (32^\circ, 24^\circ)$ for the $m_J = -1/2$ electronic Zeeman component and principal quantum number $n = 60$. Experimental data with best-fit values of temperature of 4 μK and trap depths of $U_o/k_B = 22$, 18, and 14 μK are shown as red circles, green diamonds, and blue squares, respectively, along with color-coded curves that represent the predictions of a theoretical model that take into account the state dependence of the optical potentials. The dashed gray curves correspond to a theory in which this state dependence is neglected and a single optical potential is used (that of the $m_F = 0$ sublevel). The solid gray theory curves correspond to an excitation scheme in which field Ω_1 is z polarized.

frequency difference between the Zeeman Rydberg sublevel having total magnetic quantum number m from the level having $m = 0$. For $n = 40$, the quantity ω_{m0} results primarily from the hyperfine and Zeeman interactions and the light shifts for the Rydberg sublevels can be neglected as they have an insignificant effect on the signal. The frequency ω is determined by the depth of the trap potential U_0.

To fit our data we need to know the value of the trap depth U_0 and the temperature T. We obtain values for these quantities by fitting our data with the half-wave plate angle controlling the polarization of the first excitation field set equal to $\theta_i = 0$. In this case, both the fields that constitute the two-photon excitation scheme are z polarized and $Q_{\pm 1} = 0$ in Eq. (5). The retrieved signal in this case, displayed as blue diamonds in Fig. 2, exhibits the oscillatory behavior predicted by the exponential term in Eq. (5), which can be attributed to the center-of-mass motion of the atom within the optical lattice trap potential. In fitting the data to theory, however, we allow for trap anharmonicity [see Eq. (3)] and extract values for U_0 and T from the frequency and visibility of the oscillations, respectively. A theoretical curve using the best-fit value of $U_0/k_B = 31\ \mu$K and $T = 10\ \mu$K is displayed in the figure as a solid blue curve. If the potential were purely harmonic, the signal would rephase at integral multiples of the trap frequency; however, owing to the trap anharmonicity, the oscillations are no longer purely periodic. Trap anharmonicity also adds slightly to the decay of the signal.

Having obtained values of U_0 and T, we switch the half-wave plate angle to an angle $\theta_i \neq 0$. In that case the signal oscillates at the beat frequency between the different Rydberg sublevels. Fitting the signal to the full theoretical expression given in Eq. (3) using the best-fit values of U_0 and T found previously allows us to extract the hyperfine splitting ν_{hfs}, treated as a free parameter. The quantities $Q^{(V)}_{p_J n s m_F}$ appearing in Eq. (3) are also treated as adjustable parameters in the fitting procedure to account for the uncertainties in the bandwidths, detunings, and strengths of the excitation and retrieval pulses. A representative output signal in one of the detectors is shown in Fig. 2 with experimental data points displayed as red circles and theory as the solid red curve. We find agreement between the experimental data and the best-fit models obtained via Markov chain Monte Carlo fitting. The input and output polarization angles $\theta_i = 32^\circ$ and $\theta_i = 24^\circ$ were empirically chosen to maximize the visibility of the Rydberg Zeeman beat frequency oscillations.

We have also used an alternative excitation scheme with a smaller value of k_{12} that leads to a diminished amplitude of the oscillations attributed to motion in the traps (see the dashed gray curves in Fig. 3). In this scheme atoms are optically pumped into the $|5s_{1/2}, F = 2, m_F = 2\rangle$ ground state and the $5p_{1/2}$ level is the intermediate state for two-photon excitation with fields Ω_1 and Ω_1 having wavelengths of 795 nm and 475 nm. The signal in this case is shown in Fig. 3 for $T = 4\ \mu$K and trap depths $U_0/k_B = 22$, 18, and 14 μK.

For $n = 40$, the light shifts do not significantly contribute to the separation between the three m_F Rydberg sublevels that are excited. Moreover, the *differential* optical potentials for the three states are sufficiently small to result in approximately the same motional states for the three levels. This is no longer the case for higher values of n. For example, the theoretical curves shown in Fig. 3 for $n = 60$ exhibit differences between the models assuming a single state independent potential (that associated with the $m_F = m_J + m_I = 0$ level) and the true

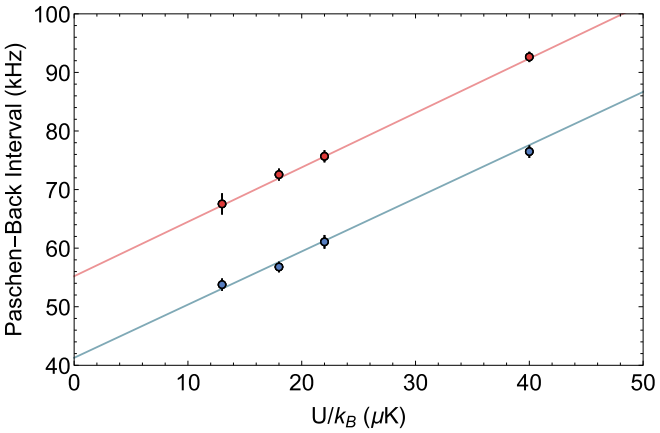

FIG. 4. Average frequency separation between adjacent nuclear-spin states within the same m_J manifold for the $n = 60$ Rydberg level as a function of trap depth for the upper ($m_J = \frac{1}{2}$, blue circles) and lower ($m_J = -\frac{1}{2}$, blue circles) electronic Zeeman manifold.

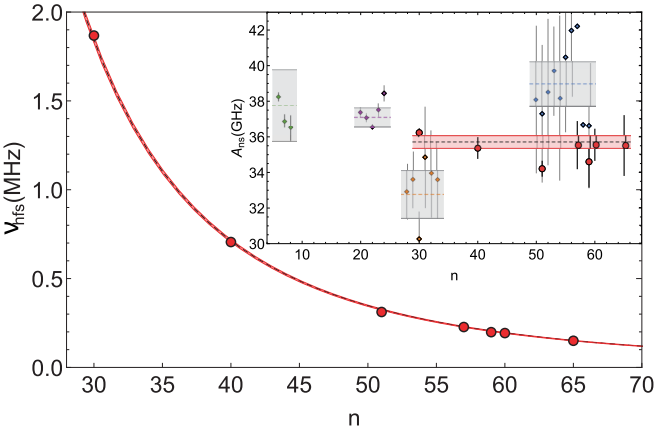

FIG. 5. Hyperfine frequency ν_{hfs} as a function of principal quantum number n. The inset depicts the same data after removing the $(n - 3.13)^{-3}$ dependence. The red band represents a 95% confidence interval for our fitted value. Gray intervals are data from Ref. [13] (green), Ref. [9] (purple), Ref. [14] (orange), and Ref. [15] (blue).

state-dependent potentials. In addition, for higher values of n, effects of spontaneous decay from the $|6p_{3/2}\rangle$ state, which is coupled to the Rydberg levels by the trap fields, add to the signal decay rate. Moreover, the dephasing associated with the breakdown of the dipole approximation in calculating the contributions of the ponderomotive potential to the light shifts also increases the decay of the signal [6]. Experimental data for $n = 60$ shown in Fig. 3 do not allow us to distinguish definitively between the state-independent and state-dependent potential models.

The measured frequency intervals as a function of trap depths are displayed in Fig. 4 for the two electronic Zeeman components of the $|60s_{1/2}\rangle$ level, together with linear fits based on Eqs. (A6) and (A26). The two intervals differ by the nuclear Zeeman interaction. The intervals in the absence of the trapping potential are determined by the intercepts of the fits with the ordinate. Using Eq. (A6) the value of the hyperfine splitting $\nu_{hfs} = 193 \pm 5$ kHz for the $n = 60$ Rydberg state is determined.

For other values of n, fits similiar to those in Fig. 2 are made for a single value of the trap depth. Each value of ν_{hfs} constitutes a weighted average of values obtained over up to three runs using data recorded by the two detectors. The mean value ν_{hfs} is computed as a weighted average of $\nu_{hfs}^{(i)}$, with the weights being their inverse variances extracted from the individual fits.

The two main sources of uncertainty for ν_{hfs} are (1) statistical errors resulting from the weighted sum of the individual values and (2) the uncertainty in the determination of the trap depth which translates into an error of the inferred differential light shifts for the hyperfine Paschen-Back states. The frequency $\nu_{hfs} \sim n^{-3}$, while differential light shifts scale as $\sim n^3$. As a result, the statistical uncertainty is the dominant one for $n = 30$ and 40, whereas the error due to the uncertainty of the trap depth is the larger one for states of $n \geqslant 51$. The data are shown in Fig. 5(a) along with a fit using $\nu_{hfs} = C(n - 3.13)^{-3}$ with C as an adjustable parameter. In the inset to Fig. 5 we plot the scaled hyperfine constant $A_{ns} \equiv \nu_{hfs}(n - 3.13)^3$. The weighted average $\overline{A}_{ns} = 35.71 \pm 0.18$GHz is plotted as a dashed line together with a corresponding 95% confidence region. Also shown are the results of prior measurements of A_{ns} [9,10,13–15].

V. CONCLUSIONS

In summary, we have analyzed nuclear-spin manifolds associated with the ns Rydberg levels of ^{87}Rb atoms placed in magnetic and optical lattice fields. Using the eigenvalues and eigenkets for the Rydberg manifold, we have investigated the dynamics of phase-matched emission following illumination of an ensemble of cold atoms with excitation and readout laser pulses. In this way, Rydberg state-dependent light shifts and hyperfine splittings for principal quantum numbers between $n = 30$ and $n = 65$ have been determined. Our results have relevance to implementations of optically trapped Rydberg qubits allowing for high-fidelity quantum gates.

ACKNOWLEDGMENTS

This work was supported by the ARL Center for Distributed Quantum Information, AFOSR, and the National Science Foundation.

APPENDIX: THEORETICAL DETAILS

1. Basis set and Hamiltonian

We consider an ns Rydberg level of ^{87}Rb subjected to a magnetic field **B** along z and a y-polarized optical trap field nearly resonant with the $|ns\rangle \leftrightarrow |6p_{3/2}\rangle$ transition frequency, as shown in Fig. 1. The trap fields counterpropagate in the x direction. The atom-field detuning between the trap field frequency and the $|ns\rangle \leftrightarrow |6p_{3/2}\rangle$ transition frequency is much larger than the Zeeman splitting of the $6p_{3/2}$ or ns sublevels. We use the $|nLSJIFm_F\rangle$ basis throughout with $S = 1/2$ and $I = 3/2$. To simplify the notation we write the state kets for the ns states as $|nFm_F\rangle$, since $L = 0$ and $J = 1/2$ for these states. We denote the zero field hyperfine separation of the ns state by $h\nu_{hfs}$ (the n label is suppressed).

In the absence of all but the Coulomb interaction, there are eight degenerate levels in an *ns* manifold, each having energy $E_n^{(0)} = \hbar\omega_{ns}$—we neglect this contribution to the Hamiltonian since it is the same for all the levels. Next there is the contribution to the Hamiltonian from the hyperfine interaction, denoted by H_{hf}. In the $|nFm_F\rangle$ basis, this contribution is diagonal and given in frequency units by

$$\frac{\langle nF'm_F'|H_{hf}|nFm_F\rangle}{h} = \nu_{hfs}\begin{cases}\frac{3}{8}\delta_{F,2}\\ -\frac{5}{8}\delta_{F,1}\end{cases}\delta_{F,F'}\delta_{m_F,m_F'}, \quad \text{(A1)}$$

where $\delta_{a,b}$ is a Kronecker delta. Finally, there is the magnetic-field interaction contribution,

$$H_B = -\frac{\beta_0 B}{\hbar}\left(g_s S_z + g_I\frac{m_e}{m_p}I_z\right), \quad \text{(A2)}$$

where β_0 is the Bohr magneton and $g_I = -0.995\times10^{-3}$ [16] is the nuclear g factor. In frequency units,

$$\frac{H_B}{h} = \frac{\beta_0 B}{h}\left(2S_z + g_I\frac{m_e}{m_p}I_z\right)/\hbar$$
$$= 1.40(\text{MHz})B(\text{G})\left(2\frac{S_z}{\hbar} + 0.995\times10^{-3}\frac{I_z}{\hbar}\right). \quad \text{(A3)}$$

The interaction Hamiltonian H_B is *not* diagonal in the $|nFm_F\rangle$ basis, with matrix elements given by

$$\langle nF'm_F'|H_B|nFm_F\rangle/h = \nu_B\sum_{m_s,m_I}\begin{bmatrix}\frac{1}{2} & \frac{3}{2} & F'\\ m_s & m_I & m_F\end{bmatrix} \quad \text{(A4)}$$

$$\times\begin{bmatrix}\frac{1}{2} & \frac{3}{2} & F\\ m_s & m_I & m_F\end{bmatrix}\left(2m_s + 0.995\times10^{-3}m_I\right)\delta_{m_F,m_F'}, \quad \text{(A5)}$$

where $\nu_B = \beta_0 B/h$ is the Larmor frequency in Hz and the quantity in square brackets is a *Clebsch-Gordan* coefficient. The modification to the eigenvalues from the nuclear term must be included because of the sensitivity of the experiment to the shift produced by this term, but the eigenkets can be calculated neglecting this contribution.

It is simple to diagonalize $H_{hf} + H_B$ since it is block diagonal. The eigenfrequencies are equal to

$$\nu_{n8} = \frac{3\nu_{hfs}}{8} + \nu_B, \quad m_F = 2,$$
$$\nu_{n7,n1} = \frac{-\nu_{hfs} \pm 4\sqrt{\nu_{hfs}^2 + 2\nu_{hfs}\nu_B + 4\nu_B^2}}{8}, \quad m_F = 1,$$
$$\nu_{n6,n2} = \frac{-\nu_{hfs} \pm 4\sqrt{\nu_{hfs}^2 + 4\nu_B^2}}{8}, \quad m_F = 0,$$
$$\nu_{n5,n3} = \frac{-\nu_{hfs} \pm 4\sqrt{\nu_{hfs}^2 - 2\nu_{hfs}\nu_B + 4\nu_B^2}}{8}, \quad m_F = -1,$$
$$\nu_{n4} = \frac{3\nu_{hfs}}{8} - \nu_B, \quad m_F = -2, \quad \text{(A6)}$$

and the eigenkets can be written as $|n\nu_{ni}m_F\rangle$, where i labels the frequency ν_{ni} of each level (these eigenkets are not written explicitly). In the limit that $\nu_B \gg \nu_{hfs}$, approximately satisfied in our experiment (Pashen-Back region), one recovers the $|m_s m_I\rangle$ eigenkets with associated energy levels $\pm h\nu_B$, corrected by $h\nu_{hfs}m_s m_I/2$ (spacing about $h\nu_{hfs}/4$). In the upper Zeeman submanifold the energy order (from highest to lowest) is $m_F = 2, 1, 0, -1$ and in the lower Zeeman submanifold it is $m_F = -2, -1, 0, 1$.

2. Optical potentials

We now need to calculate the contributions to the Hamiltonian arising from the trap field. In a paraxial approximation, the trap electric field, $\mathbf{E}(\mathbf{R}, t) = E(\mathbf{R}, t)\mathbf{u}_y$, is taken as

$$E(\mathbf{R}, t) = \tfrac{1}{4}[E_+(\rho, X)e^{ik_L X} + E_-(\rho, X)e^{-ik_L X}]e^{-i\omega_L t} + \text{c.c.}, \quad \text{(A7)}$$

where

$$E_\pm(\rho, X) = E_{\pm,0}\frac{w_{\pm,0}}{w_\pm(X)}e^{-\rho^2/w_\pm^2(X)}, \quad \text{(A8)}$$

ρ is the coordinate transverse to X, $E_{\pm,0}$ are the field amplitudes for the trap fields propagating to the right and left, $w_{\pm,0}$ are the waist radii of these fields,

$$w_\pm(X) = w_{\pm,0}\sqrt{1 + \frac{(X - X_{\pm,0})^2}{X_{\pm,r}^2}}, \quad \text{(A9)}$$

$X_{\pm,r} = \pi w_{\pm,0}^2/\lambda_L$ are Rayleigh lengths, $X_{\pm,0}$ are the positions of the foci of the beams, and $\lambda_L = 2\pi/k_L = 2\pi c/\omega_L$ is the wavelength of the trap beam. We have allowed for unbalanced beams, that is, the beams propagating in the $\pm X$ directions can have different waists and be centered at different positions.

The detuning of the trap field frequency from all the ground- to excited-state transition frequencies is sufficiently large to ensure that the optical potential is the same for all ground-state sublevels. The ground-state optical potential is

$$U_g = -\tfrac{1}{2}\alpha_g|\bar{E}(\mathbf{R})|^2, \quad \text{(A10)}$$

where

$$\left|\bar{E}(\mathbf{R})\right|^2 = \frac{1}{8}\begin{bmatrix}4E_+(\rho, X)E_-(\rho, X)\cos^2(k_L X)\\ +[E_+(\rho, X) - E_-(\rho, X)]^2\end{bmatrix} \quad \text{(A11)}$$

and α_g is the ground-state polarizabilty. The trap depth $U_0(\rho, X)$ of the ground-state optical potential is given by

$$U_0(\rho, X) = h\tilde{U}_0(\rho, X) = \tfrac{1}{4}\alpha_g E_+(\rho, X)E_-(\rho, X), \quad \text{(A12)}$$

where

$$\tilde{U}_0(\rho, X) = \frac{1}{4h}\alpha_g E_+(\rho, X)E_-(\rho, X) \quad \text{(A13)}$$

is the trap depth in frequency units. Therefore, we can write

$$\tilde{U}_g(\rho, X) = U_g(\rho, X)/h$$
$$= -\tilde{U}_0(\rho, X)\Bigg[\cos^2(k_L X)$$
$$+ \frac{[E_+(\rho, X) - E_-(\rho, X)]^2}{4E_+(\rho, X)E_-(\rho, X)}\Bigg]. \quad \text{(A14)}$$

The optical potential associated with an *ns* Rydberg level has been calculated previously [8,12] and consists of two parts. First there is the ponderomotive potential associated with the A^2 ($\mathbf{A}$ is the vector potential of the trap field) contribution to the Hamiltonian and is the same for all the levels in the

ns Rydberg manifold. Explicitly the ponderomotive potential is given by

$$U_n^{\rm pon}(\rho,X)=-\frac{|\alpha_f|}{16}\begin{bmatrix}4\theta_n E_+(\rho,X)E_-(\rho,X)\cos^2(k_LX)\\ +[E_+(\rho,X)-E_-(\rho,X)]^2\\ +2E_+(\rho,X)E_-(\rho,X)(1-\theta_n)\end{bmatrix}, \tag{A15}$$

where

$$\alpha_f=\left(-\frac{e^2}{m_e\omega_L^2}\right) \tag{A16}$$

is the free electron polarizability and θ_n is a "landscape" factor [6].

In addition to the ponderomotive contribution to the Hamiltonian, there is also the $\mathbf{A}\cdot\mathbf{p}$ contribution. Although the $\mathbf{A}\cdot\mathbf{p}$ contribution contains a sum over all intermediate states, the trap field is in near resonance with the $|ns\rangle \leftrightarrow |6p_{3/2}\rangle$ transition and we can restrict the the sum to only the hyperfine states in the $6p_{3/2}$ manifold. In that limit it makes no difference whether we use the $\mathbf{A}\cdot\mathbf{p}$ or $\mathbf{E}\cdot\mathbf{r}$ form of the interaction potential. However, the detuning of the trap field frequency from the $|ns\rangle \leftrightarrow |6p_{3/2}\rangle$ transition frequency is *not* sufficiently large to justify the neglect of the hyperfine splitting of the $6p_{3/2}$ sublevels. This results in optical potentials that are dependent on the m_F values of the *ns* Rydberg sublevels.

The interaction Hamiltonian associated with this nearly resonant contribution is denoted by H_r, having matrix elements in frequency units given by [17]

$$\frac{\langle nF'm_F'|H_r|nFm_F\rangle}{h}=\sum_{K,Q}S_{F'F}(K)\begin{bmatrix}F' & K & F\\ m_F' & Q & m_F\end{bmatrix}\varepsilon_Q^K, \tag{A17}$$

where

$$S_{F'F}(K)=\sum_H\frac{(-1)^{F'+H+K}\chi^+_{H;nF}(\rho,X)\chi^{-*}_{H;nF'}(\rho,X)}{2\pi\,\Delta_{ns,H}}\times[(2K+1)/(2F+1)]^{1/2}\begin{Bmatrix}F & F' & K\\ 1 & 1 & H\end{Bmatrix}\times\left[\cos^2(k_LX)+\frac{[E_+(\rho,X)-E_-(\rho,X)]^2}{4E_+(\rho,X)E_-(\rho,X)}\right], \tag{A18}$$

$$\chi^{\pm}_{H;nF}(\rho,X)=-\mu_{H;nF}E_{\pm}(\rho,X)/2\hbar, \tag{A19}$$

μ_{HF} is the reduced matrix element of the dipole moment operator between hyperfine states H of the $6p_{3/2}$ level and the nsF Rydberg level, the quantity in braces is a 6-J symbol,

$$\Delta_{ns,H}=\omega_L-\omega_{ns,H} \tag{A20}$$

is an atom-field detuning for the transition between hyperfine states H of the $6p_{3/2}$ level and the Rydberg level *ns*,

$$\varepsilon_Q^K=\sum_{q,q'}(-1)^{q'}\epsilon_q(\epsilon_{-q'})^*\begin{bmatrix}1 & 1 & K\\ q & q' & Q\end{bmatrix}, \tag{A21}$$

e_q are spherical components of the polarization ϵ, and

$$\epsilon_{\pm1}=\mp\frac{\epsilon_x\pm i\epsilon_y}{\sqrt{2}},\quad \epsilon_0=\epsilon_z. \tag{A22}$$

Note that the sum over H consists of the four hyperfine levels of the $6p_{3/2}$ state ($H=0,1,2,3$). For a y-polarized field ($\epsilon_x=\epsilon_z=0;\epsilon_y=1$),

$$\epsilon_{\pm1}=-\frac{i}{\sqrt{2}},\quad \epsilon_0=0, \tag{A23}$$

and

$$\epsilon_Q^K(y)=-\frac{1}{\sqrt{3}}\delta_{K,0}\delta_{Q,0}-\delta_{K,2}\left[\frac{1}{\sqrt{6}}\delta_{Q,0}+\frac{1}{2}(\delta_{Q,2}+\delta_{Q,-2})\right]. \tag{A24}$$

The reduced Rabi frequency $\chi_{H;nF}$ can be written in terms of that in the J basis as

$$\chi_{H;nF}=\chi_{6p_{3/2},ns_{1/2}}(-1)^{F+1}\sqrt{(2F+1)(2H+1)}\times\begin{Bmatrix}\frac{3}{2} & 1 & \frac{1}{2}\\ F & \frac{3}{2} & H\end{Bmatrix}, \tag{A25}$$

implying that the optical potential for each sublevel is proportional to

$$\chi^+_{6p_{3/2},ns_{1/2}}(\rho,X)\chi^{-*}_{6p_{3/2},ns_{1/2}}(\rho,X).$$

3. Rydberg level eigenfrequencies

In principle, we should now diagonalize the entire *ns* subspace. It turns out, however, that the effects of the optical potential can be treated using first-order perturbation theory if the basis eigenkets associated with the eigenvalues given in Eq. (A6) are used. That is, when we transform the optical potential to this basis, it is effectively diagonal for our experimental parameters. Using such a procedure we can write the near-resonant contribution to the energy of each level ν_{ni} of the manifold as

$$U^r_{\nu_{ni}}(\rho,X)\approx -hb_{\nu_{ni}}(\rho,X)\times\left[\cos^2(k_LX)+\frac{[E_+(\rho,X)-E_-(\rho,X)]^2}{4E_+(\rho,X)E_-(\rho,X)}\right], \tag{A26}$$

where $b_{\nu_{ni}}$ is in frequency units. The values of $b_{\nu_{ni}}$ are the diagonal elements of the H_r contribution to the Hamiltonian, when the $|nFm_F\rangle$ eigenkets are expanded in terms of the $|n\nu_{ni}m_F\rangle$ eigenkets associated with the eigenfrequencies given in Eq. (A6). The $b_{\nu_{ni}}$ values depend on the detuning of the trap fields from each of the hyperfine levels of the $6p_{3/2}$ manifold as well as the matrix elements connecting these hyperfine levels to the ground and Rydberg levels—as a consequence of the different matrix elements, the $b_{\nu_{ni}}$ are different for each of the Rydberg sublevels. The ponderomotive contribution to the energy is given in Eq. (A15).

Both the near-resonant and ponderomotive components of the Rydberg optical potentials, as well as the ground-state optical potential, contain both lattice terms proportional to $\cos^2(k_LX)$ and nonlattice contributions. The lattice potentials can result in a differential level shift for the Rydberg levels, owing to the fact that the trap depth differs for the different Rydberg sublevels. To account for this differential shift, we write $\cos^2(k_LX)=1-\sin^2(k_LX)$. The resulting terms that

are proportional to $\sin^2(k_L X)$ constitute the lattice potential and "1" contributes to the nonlattice potential.

For our magnetic-field strength of about 5 G, the two Zeeman submanifolds, each containing four of the eight sublevels of the *ns* Rydberg level, are separated by about 14 MHz. As such, the excitation fields can be chosen to excite only one of the Zeeman submanifolds. Thus we need consider only the optical potentials of four levels at a time. For magic wavelength lattices, one matches the ground- and excited-state trap potentials by a proper choice of the trap field detuning. In our case. it is *not* possible to simultaneously match the potentials for *all* the Rydberg sublevels. For a given Zeeman submanifold, we match the $m_F = 0$ potential. Using Eqs. (A14), (A15), and (A26), we find the matching condition is

$$b_{ns,m_F=0}(\rho, X) = \tilde{U}_0(\rho, X)\left(1 + \frac{|\alpha_f|}{\alpha_g}\theta_n\right), \tag{A27}$$

where the m_F value now uniquely labels the energy of a level in each Zeeman submanifold. Then the differences in the nonlattice part of excited- and ground-state potentials, written in frequency units, are

$$\begin{aligned}\tilde{D}_{nsm_F}(\rho, X) &= \tilde{U}_{nsm_F}(\rho, X) - \tilde{U}_g(\rho, X)\\ &= \tilde{U}_0(\rho, X)\frac{|\alpha_f|}{2\alpha_g}(1-\theta_n)[1+2r(\rho, X)]\\ &\quad - [b_{nsm_F}(\rho, X) - b_{ns,m_F=0}(\rho, X)][r(\rho, X)+1],\end{aligned} \tag{A28}$$

where

$$r = \frac{(E_+ - E_-)^2}{4E_+E_-}. \tag{A29}$$

The spatial variations of $\tilde{U}_0(\rho, X)$ at the different atomic positions lead to a dephasing which degrades the output signal.

The ground- and excited-state lattice potentials are approximated by

$$\tilde{U}_g(\rho, X) = \tilde{U}_{ns0}(X) \approx \tilde{U}_0(0,0)\sin^2(k_L X), \tag{A30a}$$

$$\tilde{U}_{nsm_F}(X) \approx \frac{b_{nsm_F}(0,0)}{b_{ns,m_F=0}(0,0)}\tilde{U}_0(0,0)\sin^2(k_L X). \tag{A30b}$$

The lattice potentials determine the center-of-mass motion of the atoms. Since these potentials are state dependent, the motion must be treated quantum mechanically. The spatial dependence of $\tilde{U}_0$ is neglected in calculating the motional states—that is, $\tilde{U}_0$ is evaluated at the center of the atomic cloud. The justification for this approximation is traced to the fact that the transverse width of the excitation fields is much less than that of the trap fields—the trap potential is approximately constant over the excitation volume. Even though $\tilde{U}_0$ does not vary that much over the excitation volume, it still can have an effect when it appears in *phases* for sufficiently long times—that is why such effects must be included in $\tilde{D}_{nsm_F}$.

4. Excitation scheme

The atoms are optically pumped into a *single* magnetic sublevel having angular momentum quantum number G and magnetic quantum number m_G. Counterpropagating fields incident along the x direction drive a two-photon transition from this ground state to the Zeeman manifolds of an *ns* Rydberg level. We consider only transitions into the four levels of the upper Zeeman manifold ($m_J = 1/2$). These are spectrally isolated from the lower Zeeman manifold. Transitions to the lower manifold can be treated by the same formalism. The two-photon transition is via *one* of the hyperfine levels (labeled by its angular momentum quantum number H) of an intermediate *np* state. The first of the excitation fields is nearly resonant (but still far enough from resonance to neglect any saturation effects) with the ground- to intermediate-state transition and has polarization given by $\cos\theta_i \mathbf{u}_z + \sin\theta_i \mathbf{u}_y$. The second field completes the transition to the Rydberg sublevels and is polarized in the z direction. At this point in the calculation, we neglect any motion of the atoms; that is, we assume the atoms are at fixed positions. The expressions to be derived will then be generalized to account for the motion of the atoms in the trap potentials.

a. First step

In perturbation theory and in an interaction representation, the intermediate-state amplitudes evolve approximately as

$$c_{p_J H m_H} = \frac{\Omega_1(\rho, X) f_1(t) e^{-i\Delta_{m_H,m_G}t}}{2\sqrt{2H+1}\Delta_{m_H,m_G}} P(m_G, m_H, \theta_i), \tag{A31}$$

where

$$P(m_G, m_H, \theta) = \begin{pmatrix} \cos\theta \begin{bmatrix} G & 1 & H \\ m_G & 0 & m_H \end{bmatrix} \\ +\frac{i\sin\theta}{\sqrt{2}} \begin{bmatrix} G & 1 & H \\ m_G & 1 & m_H \end{bmatrix} \\ +\frac{i\sin\theta}{\sqrt{2}} \begin{bmatrix} G & 1 & H \\ m_G & -1 & m_H \end{bmatrix} \end{pmatrix}, \tag{A32}$$

$$\Omega_1(\rho, X) = -\frac{E_1(\rho, X)}{\hbar}\langle p_J H \| \mu \| G\rangle, \tag{A33}$$

$$\Delta_{m_H,m_G} = \omega_{L_1} - \omega_{m_H,m_G}, \tag{A34}$$

$\langle p_j H || \mu || G\rangle$ is a reduced matrix element, p_J is a label for the intermediate state, ω_{m_H,m_G} is the frequency difference between the m_H hyperfine level and the m_G ground-state level, ω_{L_1} is the frequency of the first excitation field, $E_1(\rho, X)$ its amplitude, and $f_1(t)$ is its envelope function. It is assumed that the field is in near resonance with a single hyperfine level H of either the $p_J = 6p$ or $p_J = 5p$ manifolds, depending on the excitation scheme. Although in near resonance, the detunings Δ_{m_H,m_G} satisfy $\Delta_{m_H,m_G} T_{pe} \gg 1$ and $\gamma_H/(2\Delta_{m_H,m_G}) \ll 1$, where T_{pe} is the excitation pulse duration and γ_H is the decay rate of the intermediate state; as a consequence of the first inequality, the intermediate-state amplitude adiabatically follows the field amplitude. Note that Δ_{0,m_G} corresponds to Δ in Fig. 1(b). In our experiment, $\Delta/2\pi \approx 12$ MHz, $T_{pe} \approx 1.0$ μs, and the frequency spacing between the adjacent $6p_{3/2}(H=3)$ magnetic sublevels is $\approx$4.7 MHz.

b. Second step

The second excitation field, which is applied simultaneously with the first, couples each intermediate state magnetic

sublevel labeled by m_H to a single level in the upper Zeeman ($m_J = 1/2$) submanifold having the same value, $m_F = m_H$, which remains a good quantum number. Since the final states are approximate eigenstates of I_z and J_z (Paschen-Back region), it is convenient to use the $m_J m_I$ basis for these final excited states. Thus we write

$$\dot{c}_{ns,1/2,m_I} = \frac{iE_2(\rho,X)f_2(t)}{2\hbar} c_{p_J H m_H}(t) \sum_{m_H} e^{-i\Delta_{m_J m_I, H m_H} t} \times \langle ns, m_J = 1/2, m_I | \mu_z | p_J H m_H \rangle, \tag{A35}$$

where

$$\Delta_{m_J m_I, m_H} = \omega_{L_2} - \omega_{m_J m_I, m_H}, \tag{A36}$$

$\omega_{m_J m_I, m_H}$ is the frequency difference between the $nsm_J m_I$ Rydberg level and the m_H hyperfine level, ω_{L_2} is the frequency of the second excitation field, $E_2(\rho, X)$ its amplitude, and $f_2(t)$ is its envelope function. The kets $|p_J H m_H\rangle$ are expanded as

$$|p_J H m_H\rangle = \sum_{m_I', m_J'} \begin{bmatrix} J_p & 3/2 & H \\ m_J' & m_I' & m_H \end{bmatrix} \left| p_J, m_J', m_I' \right\rangle \tag{A37}$$

and substituted into Eq. (A35). In the resulting expression, only those matrix elements having $m_J' = m_J = 1/2$ and $m_I' = m_I$ contribute in Eq. (A35); as a consequence, we find

$$\dot{c}_{ns,1/2,m_I} = -i \frac{\Omega_2(\rho,X)\Omega_1(\rho,X) f_1(t) f_2(t)}{4\sqrt{2p_J+1}\sqrt{2H+1}} \times e^{-i\Delta_{m_J m_I, m_G} t} \sum_{m_H} \frac{P(m_G, m_H, \theta_i)}{\Delta_{m_H, m_G}} \times \begin{bmatrix} J_p & 1 & 1/2 \\ 1/2 & 0 & 1/2 \end{bmatrix} \begin{bmatrix} J_p & 3/2 & H \\ 1/2 & m_I & m_H \end{bmatrix}, \tag{A38}$$

where J_p is the angular momentum of the intermediate p state,

$$\Omega_2(\rho, X) = -\frac{E_2(\rho,X)}{\hbar} \langle ns_{1/2} \| \mu \| p_J \rangle, \tag{A39}$$

$$\Delta_{m_J m_I, m_G} = \omega_{L_1} + \omega_{L_2} - \omega_{m_J m_I, m_G}, \tag{A40}$$

$\omega_{m_J m_I, m_G}$ is the frequency difference between the $nsm_J m_I$ Rydberg level and the m_G ground level, and we have used Eq. (A31). If we define

$$K(m_G, m_H, m_J, m_I) = \frac{P(m_G, m_H, \theta_i)}{\Delta_{m_H, m_G}} \times \int_{-\infty}^{\infty} dt\, f_1(t) f_2(t) e^{-i\Delta_{m_J m_I, m_G} t}, \tag{A41}$$

then

$$c_{1/2,m_I}(0^+) = -\frac{i\Omega_2(\rho,X)\Omega_1(\rho,X)}{4\sqrt{2H+1}\sqrt{2J_p+1}} \times \sum_{m_H} K(m_G, m_H, 1/2, m_I) \times \begin{bmatrix} J_p & 1 & 1/2 \\ 1/2 & 0 & 1/2 \end{bmatrix} \begin{bmatrix} J_p & 3/2 & H \\ 1/2 & m_I & m_H \end{bmatrix}, \tag{A42}$$

where $0+$ is a time immediately following the excitation pulses. Only a single term, one having $m_H = 1/2 + m_I$, enters the sum—that is, each intermediate state is coupled only to a single final state in the upper Zeeman manifold having the same value of m_F. A specific example is given below in Sec. 7.

5. Retrieval pulse

The excitation pulses create coherence $\rho_{Gm_G, nsm_J m_I}$ between the ground Gm_G level and the $nsm_J m_I$ Rydberg sublevels. The relative values of $\rho_{Gm_G; nsm_J m_I}$ for different $m_J m_I$ are determined by the polarization of the excitation fields. To monitor this coherence, a retrieval pulse, polarized in the z direction and propagating in the same direction as the second excitation field, is applied at a time T_s following the excitation pulses. The field is resonant with the same Rydberg–intermediate-state transition used in the excitation process . The retrieval pulse creates coherences $\rho_{Gm_G; p_J H m_H}$ which lead to phase-matched emission on the ground- to intermediate-state transition in the same direction as the first excitation field. In general, this emission will have polarization components in both the y and z directions.

The retrieval pulse drives transitions between states having the same value of m_F. The appropriate equations of motion are

$$\dot{c}_{p_J H m_H} = -\frac{\gamma_H}{2} c_{p_J H m_H} + \frac{iE_r(\rho,X) f_r(t - T_s)}{2\hbar} e^{i\Delta^r_{m_H; 1/2, m_J} t} \times \langle p_J H m_H | \mu_z | nsm_J m_I \rangle c_{m_J m_I}, \tag{A43}$$

where

$$\Delta^r_{m_H, m_J m_I} = \omega_{L_r} - \omega_{m_J m_I, m_H}. \tag{A44}$$

ω_{L_r} is the frequency of the retrieval pulse, $E_r(\rho, X)$ its amplitude, and $f_r(t - T_s)$ is its envelope function. The field frequency can be chosen to ensure that $\Delta^r_{m_H, m_J m_I} = 0$ for a given value of m_H but, owing to the Zeeman splitting in the intermediate state, it cannot be equal to zero for *all* values of m_H. In the main text, the retrieval pulse is represented by the symbol Ω_A.

Following the same procedure we used for the excitation field, we find

$$\dot{c}_{p_J H m_H} = -\frac{\gamma_H}{2} c_{p_J H m_H} - i \frac{\Omega_r(\rho,X)}{2\sqrt{2J_p+1}} f_r(t - T_s) e^{i\Delta^r_{m_H; 1/2, m_H - 1/2} t} \times \begin{bmatrix} J_p & 1 & 1/2 \\ 1/2 & 0 & 1/2 \end{bmatrix} \begin{bmatrix} J_p & 3/2 & H \\ 1/2 & m_H - 1/2 & m_H \end{bmatrix} \times c_{ns,1/2,m_H - 1/2}, \tag{A45}$$

where

$$\Omega_r(\rho, X) = -\frac{E_r(\rho,X)}{\hbar} \langle p_J \| \mu \| ns_{1/2} \rangle. \tag{A46}$$

In contrast to the excitation pulse, the duration of the retrieval pulse is greater than γ_H^{-1}; moreover, its Rabi frequency is typically larger than γ_H so as to collect the output signal on a time scale of order γ_H^{-1}. As such, a perturbation treatment is no longer valid and Eq. (A45) must be solved numerically along with the corresponding equation for $\dot{c}_{nsm_J m_I}$. This solution provides values for $c_{p_J H m_H}(t)$ in terms of $c_{nsm_J m_I}(0^+)$, which

can be used to calculate the radiated signal. Since we are considering only a single Zeeman submanifold with $m_J = 1/2$ and a single value of H, there is no sum in Eq. (A45). Only a single value of H and $m_I = m_H - 1/2$ are present in the equation. If we write

$$\Delta^r_{m_H;1/2,m_H-1/2}t = \Delta^r_{m_H;1/2,m_H-1/2}T_s + \Delta^r_{m_H;1/2,m_H-1/2}(t-T_s), \tag{A47}$$

then the formal solution of Eq. (A45) is given by

$$c_{p_JHm_H}(t) = R_{p_JHm_H;nsm_Jm_I}(t-T_s)e^{i\Delta^r_{m_H;1/2,m_H-1/2}T_s} \times c_{nsm_Jm_I}(0^+)\delta_{m_J,1/2}\delta_{m_I,m_H-1/2}. \tag{A48}$$

In all but the perturbation theory limit, $R_{p_JHm_H;nsm_Jm_I}(t-T_s)$ is a nonlinear function of Ω_r. The interaction representation density-matrix element,

$$\rho^I_{p_JHm_H;Gm_G}(t) \approx c_{p_JHm_H}(t), \tag{A49}$$

since the initial state amplitude is unchanged in lowest-order perturbation theory.

So far the calculations have been carried out for an atom located at $X = 0$. To generalize Eq. (A49) for an atom located at $X = X_j$, we set

$$\rho^{I(j)}_{p_JHm_H;Gm_G}(t) \approx c_{p_JHm_H}(t)e^{ik_0X_j}, \tag{A50}$$

where $k_0 = \omega_{HG}/c = \omega_{L_r}/c$.

6. Signal

The excitation, readout, and vacuum fields combine to produce a phase-matched emission in the $\mathbf{u}_x$ direction. The output electric field in the phase-matched direction has both y and z polarization components. These components are mixed on a half-wave plate oriented at an angle $\theta_d/2$ from the z axis to produce new vertical and horizontal components given by

$$\begin{aligned} E_V &= E_z\cos\theta_d + E_y\sin\theta_d, \\ E_H &= E_y\cos\theta_d - E_z\sin\theta_d, \end{aligned} \tag{A51}$$

which are then separated by a polarizing beam splitter and measured in two detectors. We discuss only the vertical component signal—the horizontal component signal can be obtained by interchanging $\cos\theta_d$ with $-\sin\theta_d$ and $\sin\theta_d$ with $\cos\theta_d$ in the final result.

The time-integrated phase-matched signal recorded at the vertical detector is proportional to a quantity S_V defined by

$$S_V(T_s) = X_d^2\int dt\,\langle E_{V+}(X_d,t)E_{V-}(X_d,t)\rangle, \tag{A52}$$

where $E_{V\pm}(X_d,t)$ are the positive and negative frequency components of the vertical component of the electric-field operator evaluated at some arbitrary point X_d in the radiation zone to the right of the half-wave plate. Using source-field theory [18], it then follows that

$$S_V(T_s) = \int_0^\infty dt|G_V(X_d,t)|^2, \tag{A53}$$

where

$$\begin{aligned} G_V(X_d,t) &= \frac{\omega_0^2}{4\pi\epsilon_0c^2}\sum_{m_H}e^{-i\omega_{m_Hm_G}(t-X_d/c)}\langle Gm_G|(\mu_z\cos\theta_d+\mu_y\sin\theta_d)|p_JHm_H\rangle\sum_{j=1}^N\rho^{I(j)}_{p_JHm_H,Gm_G}(t-X_d/c)e^{-ik_0X_j} \\ &= \left(\frac{\omega_0^2}{4\pi\epsilon_0c^2}\right)\frac{\langle p_JH\|\mu\|G\rangle^*}{\sqrt{2H+1}}\sum_{m_I=-3/2}^{3/2}e^{i(\omega_{Lr}-\omega_{1/2,m_I;m_G})T_s}P(m_G,m_I{+}1/2,\theta_d)\sum_{j=1}^N R^{(j)}_{p_JHm_I+1/2;ns,1/2,m_I}(t-T_s-X_d/c) \\ &\quad\times e^{-i\omega_{H,m_I+1/2;Gm_G}(t-T_s-X_d/c)}c^{(j)}_{ns,1/2,m_I}(0^+), \end{aligned} \tag{A54}$$

and Eqs. (A48) and (A50) have been used. The spatial phase factors of the excitation fields have been accounted for in Eq. (A50), so that the only spatial dependence of $c^{(j)}_{ns,1/2,m_I}(0^+)$ on j is related to the fact that the excitation field envelopes, $E_{1,2}(\rho,X)$, are a function of position in the atomic cloud. By combining the numerical solution leading to Eq. (A48) with Eq. (A42), it is possible to calculate $G_V(X_d,t)$ and $S_V(T_s)$.

Modifications resulting from the trap potentials

The trap potentials lead to a number of qualitatively different effects that modify the signal intensity. Of primary concern to us is the motional dephasing that occurs between the excitation and readout pulses. By using matched trap potentials for both the ground and Rydberg levels, the motional dephasing can be reduced significantly from a case in which the atoms undergo force-free motion. Since it is not possible to match all the Rydberg sublevel potentials to the ground-state potential, there is some slight dephasing that results from the potential differences as a result of the spatial dependence of the fields in the atomic cloud. This is in addition to a similar dephasing that occurs for high n Rydberg levels associated with the ponderomotive potential.

To generalize the result to include the effects of the trap potentials, we make a number of simplifying assumptions. First, we assume that atomic motion is frozen during the excitation and retrieval pulses. For our trap depths and temperatures, this is generally a very good approximation. Second, we approximate the energy levels in each potential as those associated with the quasibound states of the corresponding Mathieu equation problem [19]. Although we use the Mathieu equation quasibound eigenenergies (since they appear in phases), we calculate transition matrix elements using harmonic-oscillator wave functions, assuming the atoms are sufficiently cold to be localized near the bottom of the wells. As was already

mentioned, we neglect any spatial variations of the field in calculating the quasibound states in the potentials—all fields are evaluated at cloud center, but we include the spatial variations of the fields insofar as they affect light shifts of the Rydberg levels relative to those of the ground state.

With these approximations and assuming an initial density matrix that is diagonal with respect to the motional states, we find [8,12] that $G_V(X_d,t)$ can be written as

$$\begin{aligned} G_V(X_d,t) = {} & e^{i(\omega_{Lr}+\omega_{Gm_G})T_s} e^{-\Gamma_{ns}T_s/2}\Theta(t-T_p-X_d/c) \\ & \times \sum_{m_F=-1}^{2}\sum_{q,q'}^{q_{\max}}\sum_{j=1}^{N} Q^{(V)(j)}_{p_J H m_H=m_F;nsm_F}(t-T_p-X_d/c) \\ & \times e^{-2\pi i\tilde{D}^{(j)}_{nsm_F}T_s} M_{gq;nsm_Fq'}(-k) \\ & \times M_{nsm_Fq';gq}(k) e^{i(\omega_q^{(g)}-\omega_{q'}^{(nsm_F)})T_s}\rho_{1q,1q}(0), \end{aligned} \tag{A55}$$

where

$$\begin{aligned} M_{nsm_Fq;gq'}(k) &= \int dX[\psi_{nsm_Fq}(X)]^* e^{ikX}\psi_{gq'}(X) \\ &= [M_{gq';nsm_Fq}(-k)]^*, \end{aligned} \tag{A56}$$

$\psi_{\alpha q}(X)$ is a ground-state eigenfunction and $\omega_q^{(g)}$ an eigenfrequency for an atom moving in the potential $U_g(0,0)$, $\psi_{nsm_Fq}(X)$ is an eigenfunction and $\omega_q^{(nsm_F)}$ an eigenfrequency for an atom moving in the potential $U_{nsm_F}(0,0)$, and $\tilde{D}^{(j)}_{nsm_F}$ is given by Eq. (A28). The function $Q^{(V)(j)}_{p_JHm_H;nsm_F}(t)$ incorporates all the excitation and retrieval dynamics. The sums over q,q',q'' are restricted to (quasibound) states; that is, $q_{\max}$ is the number of bound states in the potential. A loss factor, $e^{-\Gamma_{ns}T_s/2}$, has been added to allow for decay between the excitation and retrieval pulses owing to spontaneous emission, blackbody radiation, and decay from the intermediate state. The sum over j actually corresponds to an integral over X and ρ, taking into account the spatial dependence of the excitation and retrieval fields, weighted with the atomic density distribution.

For the polarizations of our excitation fields, the sum over m_F consists of at most three terms, $m_F = m_G, m_{G\pm1}$. Experimentally, we optically pump the initial state into $m_G = 0$, so only Rydberg levels having $m_F = 0,\pm1$ are populated.

The numerical calculation of $S_V(T_s)$ is time consuming, since the sum over j in Eq. (A53) must be carried out for each $\tau = t - T_p - X_d/c$, the result squared, and then integrated over τ from zero to infinity. To simplify matters, we assume that

$$Q^{(V)(j)}_{p_JHm_H=m_F;nsm_F}(\tau) \approx Q^{(V)}_{p_Jnsm_F} g(\tau)\Lambda(\rho,X), \tag{A57}$$

where $g(\tau)$ is a state independent function of τ and

$$\Lambda(\rho,X) = \Omega_r(\rho,X)\Omega_2(\rho,X)\Omega_1(\rho,X). \tag{A58}$$

While this approximation is not justified in general, it should not seriously affect the dependence of the *normalized* signal on T_s. With this assumption, the signal at time T_s normalized to that at $T_s = 1\ \mu$s can be written in the form given in Eqs. (1)–(3). In those expressions, the sum over j has been converted to a spatial integral over the sample.

For example, if $G = 2$ and $m_G = 0$, the basic structure consists of the absolute square of the sum of three terms oscillating at the frequencies of the $m_F = 0,\pm1$ Rydberg levels. The signal then oscillates at the difference frequencies of these levels. With our knowledge of the potential, we are then able to extract the hyperfine constant from the signal.

7. Perturbation theory calculation of $C_V(\rho, X, T_s)$

In this section, we give perturbation theory expressions for $c_{m_Jm_I}(0^+)$, $c_{p_Jm_H}(t)$, and $C_V(\rho,X,T_s)$ when $G = 2$, $m_G = 0$, $J_p = 3/2$, $m_J = 1/2$, and $H = 3$ (values appropriate to one of the excitation schemes in our experiment). For these values, it follows from Eqs. (A42) and (A60) that

$$\begin{aligned} c_{1/2,1/2}(0^+) &= -\frac{\Omega_2(\rho,X)\Omega_1(\rho,X)}{40\sqrt{7}}K(1/2)\sin\theta_i, \\ c_{1/2,-1/2}(0^+) &= \frac{3i\Omega_2(\rho,X)\Omega_1(\rho,X)}{80\sqrt{7}}K(-1/2)\cos\theta_i, \\ c_{1/2,-3/2}(0^+) &= -\frac{\Omega_2(\rho,X)\Omega_1(\rho,X)}{40\sqrt{21}}K(-3/2)\sin\theta_i, \end{aligned} \tag{A59}$$

where

$$K(m_I) = \frac{\int_{-\infty}^{\infty} dt\, f_1(t) f_2(t) e^{-i\Delta_{1/2,m_I;0}t}}{\Delta_{m_I+1/2,0}}. \tag{A60}$$

If all the K's were equal (which would be the case if the Zeeman splitting of the intermediates state is much larger than the detuning $\Delta_{m_H,0}$ and if $|\Delta_{1/2,m_I;0}T_{pe}| \ll 1$, as it is for most of the n in our experiment), then

$$\begin{aligned} c_{1/2,-3/2}(0^+) &= c_{1/2,1/2}(0^+)/\sqrt{3}, \\ c_{1/2,-1/2}(0^+) &= -3i\,\cot\theta_i c_{1/2,1/2}(0^+)/2. \end{aligned} \tag{A61}$$

Note that the relative coherence between the $c_{1/2,-3/2}$ and $c_{1/2,-1/2}$ is important since it leads to the y-polarized signal in the phase-matched direction.

We next solve Eq. (A45) using perturbation theory for a square envelope retrieval pulse for which

$$f_r(\tau) = \begin{cases} 0, & \tau < 0 \text{ and } \tau > T_{pr}, \\ 1, & 0 < \tau < T_{pr}, \end{cases} \tag{A62}$$

assuming that $\gamma_H T_{pr} \gg 1$ (T_{pr} is the retrieval pulse duration), to obtain

$$c_{p_JHm_H}(t) \approx -i\frac{\Omega_r(\rho,X)}{4}\frac{e^{i\Delta^r_{p_JHm_H;ns,1/2.m_H-1/2}T_s}}{\frac{\gamma_H}{2}+i\Delta^r_{p_JHm_H;ns,1/2.m_H-1/2}}\begin{bmatrix}3/2 & 1 & 1/2\\ 1/2 & 0 & 1/2\end{bmatrix}\begin{bmatrix}3/2 & 3/2 & 3\\ 1/2 & m_H-1/2 & m_H\end{bmatrix}c_{ns,1/2,m_H-1/2}(0^+). \tag{A63}$$

Using Eqs. (A53)–(A58), we then find that the normalized signal, as defined in Eq. (1), is given by Eq. (2) with

$$C_V(\rho, X, T_s) = \sum_{m_F=-1}^{1} \sum_{q,q'}^{q_{\max}} e^{-i\omega_{nsm_F} T_s} Q^{(V)}_{p_J nsm_F} e^{-2\pi i \tilde{D}^{(j)}_{nsm_F}(\rho,X)T_s} M_{gq;nsm_F q'}(-k) M_{nsm_F q';gq}(k) e^{i(\omega_q^{(g)} - \omega_{q'}^{(nsm_F)})T_s} \rho_{1q,1q}(0) \tag{A64}$$

and

$$Q^{(V)}_{p_J nsm_F} = \frac{K(m_F - 1/2)}{\frac{\gamma_H}{2} + i\Delta^r_{p_J H m_H; nsm_F}} \begin{pmatrix} \sin\theta_i \sin\theta_d \delta_{m_F,1} \\ -\frac{9\cos\theta_i \cos\theta_d}{4} \delta_{m_F,0} \\ +\frac{\sin\theta_i \sin\theta_d}{3} \delta_{m_F,-1} \end{pmatrix}. \tag{A65}$$

Note that, owing to the definition given in Eq. (1), we were able to remove any spatially independent common factors in writing the expression for $Q^{(V)}_{p_j nsm_F}$.

[1] M. Saffman, T. G. Walker, and K. Mølmer, Quantum information with Rydberg atoms, Rev. Mod. Phys. **82**, 2313 (2010).

[2] M. S. Safronova, C. J. Williams, and C. W. Clark, Optimizing the fast Rydberg quantum gate, Phys. Rev. A **67**, 040303(R) (2003).

[3] M. Saffman and T. G. Walker, Analysis of a quantum logic device based on dipole-dipole interactions of optically trapped Rydberg atoms, Phys. Rev. A **72**, 022347 (2005).

[4] A. Zhang, F. Robicheaux, and M. Saffman, Magic-wavelength optical traps for Rydberg atoms, Phys. Rev. A **84**, 043408 (2011).

[5] L. Li, Y. O. Dudin, and A. Kuzmich, Entanglement between light and an optical atomic excitation, Nature (London) **498**, 466 (2013).

[6] T. Topcu and A. Derevianko, Intensity landscape and the possibility of magic trapping of alkali Rydberg atoms in infrared optical lattices, Phys. Rev. A **89**, 023411 (2014).

[7] E. A. Goldschmidt, D. G. Norris, S. B. Koller, R. Wyllie, R. C. Brown, J. V. Porto, U. I. Safronova, and M. S. Safronova, Magic wavelengths for the 5s-18s transition in rubidium, Phys. Rev. A **91**, 032518 (2015).

[8] J. Lampen, H. Nguyen, L. Li, P. R. Berman, and A. Kuzmich, Long-lived coherence between ground and Rydberg levels in a magic wavelength lattice, Phys. Rev. A **98**, 033411 (2018).

[9] A. Tauschinsky, R. Newell, H. B. van Linden van den Heuvell, and R. J. C. Spreeuw, Measurement of ^{87}Rb Rydberg-state hyperfine splitting in a room-temperature vapor cell, Phys. Rev. A **87**, 042522 (2013).

[10] J. B. Naber, A. Tauschinsky, H. B. van Linden van den Heuvell, and R. J. C. Spreeuw, Electromagnetically induced transparency with Rydberg atoms across the Breit-Rabi regime, Scipost. Phys. **2**, 015 (2017).

[11] H. Sassmannshausen, F. Merkt, and J. Deiglmayr, High-resolution spectroscopy of Rydberg states in an ultracold cesium gas, Phys. Rev. A **87**, 032519 (2013).

[12] P. R. Berman, H. Nguyen, and A. Kuzmich, Theory of coherent optical transients with quantized atomic motion, Phys. Rev. A **99**, 013427 (2019)

[13] A. Corney, *Atomic and Laser Spectroscopy* (Oxford University Press, Oxford, 1977).

[14] W. Li, I. Mourachko, M. W. Noel, and T. F. Gallagher, Millimeter-wave spectroscopy of cold Rb Rydberg atoms in a magneto-optical trap: Quantum defects of the ns, np, and nd series, Phys. Rev. A **67**, 052502 (2003).

[15] D. Meschede, Centimeter-wave spectroscopy of highly excited rubidium atoms, J. Opt. Soc. Am. B **4**, 413 (1987).

[16] D. A. Steck, http://steck.us/alkalidata.

[17] B. Dubetsky and P. R. Berman, $\lambda/4$, $\lambda/8$, and higher order atom gratings via Raman transitions, Laser Phys. **12**, 1161 (2002).

[18] P. R. Berman and V. S. Malinovsky, *Principles of Laser Spectroscopy and Quantum Optics* (Princeton University Press, Princeton , NJ, 2011), Chap. 19.

[19] See, for example, T. R. Carver, Am. J. Phys. **39**, 1225 (1971); K. Ochs, Eur. J. Phys. **32**, 479 (2011).